Editors' Suggestion

Electron time-of-flight: A new tool in β-decay spectroscopy

C. Roick,[1] D. Dubbers,[2,*] B. Märkisch,[1,†] H. Saul,[1] and U. Schmidt[2]
[1]*Physik-Department, Technische Universität München, James-Franck-Straße 1, 85748 Garching, Germany*
[2]*Physikalisches Institut, Universität Heidelberg, Im Neuenheimer Feld 226, 69120 Heidelberg, Germany*

(Received 1 September 2017; revised manuscript received 17 November 2017; published 7 March 2018)

We show that electron time-of-flight can be a useful tool in β-decay spectroscopy, even in the energy range up to 700 keV relevant for neutron β decay. As a first application, we use electron time-of-flight measurements for the precise calibration of an electron detector.

DOI: 10.1103/PhysRevC.97.035502

I. INTRODUCTION

Many experiments on neutron and nuclear β decay search for new phenomena beyond the present standard model. In favorable cases, experiments in the field of low-energy particle physics reach limits on new physics that are similar to or better than corresponding limits from high-energy physics, for recent reviews see Refs. [1–6]. In neutron decay, as an example, recent high statistics experiments [7–9] create a need for the development of improved methods of detector characterization.

In this context, we investigated the use of electron time-of-flight (ToF) for studies in β decay. In the past, electron ToF has played no role in β-decay experiments, because ToF requires a long distance between source and detector, leading to a small solid angle of detection. To increase the solid angle, one can use a magnetic field to guide the electrons from the source to the detector. Many β-decay experiments use such guiding fields. Unfortunately, when the electrons gyrate about the magnetic field, their flight times depend not only on energy, but also on the angle of electron emission, and the two quantities cannot be disentangled. Furthermore, ToF requires a start signal from a detector near the source.

Several ToF applications are possible that overcome this problem, using uniform or nonuniform magnetic fields, as was discussed in Ref. [10]. Here we use a nonuniform field configuration for electron spectroscopy, which we call the inverse magnetic mirror configuration (as shown below in Fig. 1), which makes ToF almost independent of emission angle. As a first application, we use ToF for the energy calibration of a plastic scintillator. Such scintillators are widely used in nuclear and particle physics. From the measured ToF, we calculate the kinetic energy of the electrons, and compare this energy with the size of the signal measured in the energy-sensitive scintillator. Detector calibration by ToF is complementary to conventional calibration with conversion electrons of known energy: ToF offers high resolution at lower energies, where flight times are long, whereas calibration with conversion electrons has large errors at low energies.

Up to now, electron time-of-flight methods were limited to energies of several keV. An example is photoelectron spectroscopy, which uses ToF for electron energies of order 1 eV–10 keV in magnetic bottle spectrometers, as the inverse bottle configuration is often (and somewhat imprecisely) called [11–13]. Similar field configurations are found in the first half of so-called β-retardation spectrometers such as aSPECT [14] or KATRIN [15]. The aSPECT spectrometer measures electron-neutrino correlations in neutron decay (no electron ToF). The KATRIN spectrometer searches for a nonzero neutrino mass near the 18 keV endpoint energy of tritium decay, and electron ToF measurements were done in a proof of principle experiment [16], see also Ref. [17]. In a different approach, an electron ToF spectrometer for energies below 100 keV was tested in 1984 [18] using electrons with long trochoidal trajectories in a rotationally symmetric field with radial $1/r^2$ dependence, but this method apparently has never been followed up. Finally, in previous experiments on electron, proton, and antineutrino asymmetries in neutron decay [7,19–21], electron ToF cuts were used merely to identify the initial direction of electron emission, in order to assign backscattering events to a specific detector. For highly relativistic electrons, on the other hand, with energies far above the electron rest mass of 511 keV, hence with velocities $v \approx c$, flight times are nearly independent of energy and cannot be used to measure particle energies.

At present, a large new neutron decay spectrometer named PERC is under construction by a Munich-Vienna-Heidelberg-Mainz-Grenoble collaboration [22,23], to be installed at the FRM-II reactor neutron source of the Maier-Leibnitz Center of the Technical University Munich. It consists of an 8 m long section of low and uniform solenoidal magnetic field (up to 1.5 T), followed by a short section of high field (up to 6 T), and therefore it will provide the required inverse magnetic mirror configuration. It turns out that with this field configuration, which had been selected for other reasons, electron ToF can become a useful tool for *in situ* characterization of electron detectors. Such characterization by ToF using PERC may include

(i) Detector energy calibration in an inverse magnetic mirror configuration, as described in the present article.

*dubbers@physi.uni-heidelberg.de
†maerkisch@ph.tum.de

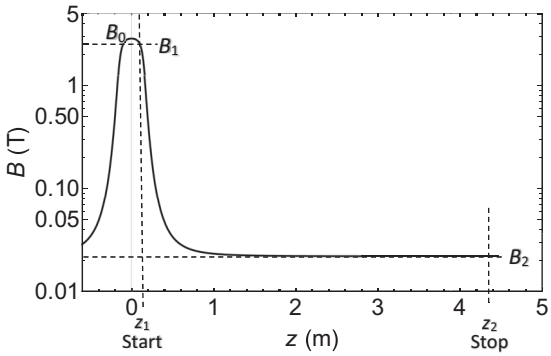

FIG. 1. Magnetic field profile $B(z)$ of our inverted magnetic mirror, with peak field $B_0 = 3\,\mathrm{T}$. The start detector and the source are at position z_1 where $B_1 = 2.5\,\mathrm{T}$, the stop detector at z_2 where $B_2 = 22\,\mathrm{mT}$.

(ii) Measurement of detector response as a function of the electron angle of incidence, in a symmetric solenoidal field configuration.
(iii) A complete experiment on electron backscattering in a uniform magnetic field.

For more details, see Ref. [10].

Section II presents the method of electron spectroscopy by ToF in an inverse magnetic mirror. Section III describes a prototype apparatus built to prove the feasibility of detector calibration by ToF, using a setup smaller than the full PERC spectrometer. Section IV presents the measured data and their evaluation, from which the energy response curve of a plastic scintillator is derived.

II. ToF SPECTROSCOPY IN NONUNIFORM FIELDS

To use electron ToF for the energy calibration of a detector, we must eliminate the strong dependence of the path lengths of the gyrating electrons on their emission angle. To this end, we choose a guiding field in an inverse magnetic mirror configuration: we place the electron source in a high magnetic field of short length, with some start detector nearby. In contrast, the long main electron flight path and, at its end, the stop detector, are in a low magnetic field, with a smooth transition between both fields. When the electrons reach the low field region, their angular distribution is strongly narrowed by adiabatic invariance. Consequently, the effective length of electron flight paths becomes nearly independent of emission angle, and so does the electron ToF.

Figure 1 shows our magnetic field distribution, which is similar to that foreseen with PERC, but with lower field and of half its length. By the inverse magnetic mirror effect, an electron will, on its trajectory along the decreasing field $B(z)$, increase its longitudinal velocity component v_z at the expense of its transverse components v_x and v_y, its amplitude v being a constant of the motion. Thereby, the angle $\theta = \arccos(v_z/v)$ between the velocity vector and the z axis will continuously diminish on the electron's flight along $B(z)$. From the adiabatic condition follows that this angle is related to the local field value $B(z)$ and the initial polar emission angle θ_1 of the electron at field B_1 as

$$\sin\theta(z) = \sqrt{B(z)/B_1}\,\sin\theta_1. \tag{1}$$

For the field configuration of Fig. 1, even for the case of electron emission under right angles $\theta_1 \approx 90^\circ$, the angle $\theta(z)$ rapidly diminishes along z, down to $\theta_2 = 5.3^\circ$ in the field $B_2 = 22\,\mathrm{mT}$, where $\cos\theta_2 = 0.996$.

The initial radius of electron gyration is $r_1 = r_{10}\,\sin\theta_1$, with the maximum gyration radius $r_{10} = p/eB_1$, and electron momentum

$$p = c\sqrt{E(E + 2mc^2)}, \tag{2}$$

with electron kinetic energy E and rest mass m. While the electron's angle θ from Eq. (1) decreases during adiabatic transport through the field $B(z)$, its gyration radius increases as

$$r(z) = \sqrt{B_1/B(z)}r_1. \tag{3}$$

With $B(z)$ from Fig. 1, electrons with, for example, $E = 500\,\mathrm{keV}$ start with maximum gyration radius $r_{10} = 1.1\,\mathrm{mm}$ at position z_1, and end with maximum radius $r_{20} = 12.3\,\mathrm{mm}$ at position z_2. With no field applied, the direct ToF of an electron from the source to the detector is

$$T_0 = z_0/v, \tag{4}$$

with the distance from the source to the stop detector $z_0 = z_2 - z_1$, and with the velocity v obtained from the relation $\beta = v/c = cp/W$, with total energy $W = E + mc^2$, or

$$v = c\sqrt{E(E + 2mc^2)}/(E + mc^2). \tag{5}$$

In a uniform magnetic guiding field B, the flight time T of an electron over a distance z_0 along B is

$$T = \ell_0/v = z_0/(v\,\cos\theta), \tag{6}$$

where $\ell_0 = z_0/\cos\theta$ is the electron's path length, and θ its emission angle.

With a radially symmetric nonuniform guiding field $B(z)$ along z, the electron flight time is replaced by the integral along axis z

$$T = \ell/v = \int_{z_1}^{z_2} dz/v_z(z), \tag{7}$$

with $v_z(z) = v\cos\theta(z)$. Using Eq. (1) (dropping the index 1 on the initial emission angle θ), the electron path length becomes

$$\ell(\theta) = \int_{z_1}^{z_2} dz/\sqrt{1 - [B(z)/B_1]\,\sin^2\theta}. \tag{8}$$

In the adiabatic approximation, there is no need to bother with electron gyration in the plane perpendicular to the field axis.

Figure 2 shows this flight length ℓ as a function of θ (solid line), calculated for the field profile $B(z)$ of Fig. 1. The strong dispersion of path lengths in the uniform field case (dotted line, diverging for $\theta \to 90^\circ$) almost completely disappears. Even for emission under $\theta = 90^\circ$, electron paths have nearly the same length as for emission under $\theta = 0^\circ$, which is $z_0 = 4.452\,\mathrm{m}$ (dashed line). The tiny residual dispersion of path

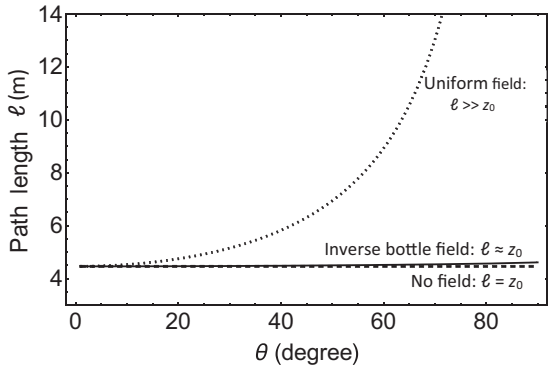

FIG. 2. Electron path length ℓ as a function of emission angle θ. Dotted curve: for a uniform guiding field, the length of the electron trajectories $z_0/\cos\theta$ reaches 14 m for $\theta = 70^\circ$ and diverges for $\theta = 90^\circ$. Dashed line: with no guiding field, for direct flight to a distant detector, all flight paths have the same length $\ell = z_0 = 4.452$ m. Solid line: for the inverse bottle field of Fig. 1, all path lengths from Eq. (8) are nearly the same, $\ell \approx z_0$, even for electron emission at $\theta = 90^\circ$.

lengths seen in the figure lead to small shifts und additional broadening of the flight times T.

The adiabatic condition requires that the change of the magnetic field $B(z)$ along z is small during one cycle of the helical motion of the charged particle. From this follows that adiabatic transport is guaranteed for a small adiabatic parameter

$$\eta = \frac{2\pi p}{eB^2}\left|\frac{dB}{dz}\right| \ll 1. \tag{9}$$

For our setup, for $E = 500$ keV, the adiabatic parameter η reaches a maximum of 0.76, see Fig. 3, as calculated from the measured field map. This maximum does not occur at the edge of the solenoid at $z = 0.15$ m where the axial field gradient dB/dz is steepest, but at $z = 0.23$ m within the opening of the iron yoke of the magnet shown in Fig. 4. Possible effects due to nonadiabaticity will be discussed in Sec. IV D. In any case, such large values for η will not occur in PERC, see Ref. [23], where, as in all neutron decay instruments, adiabaticity of particle transport is crucial.

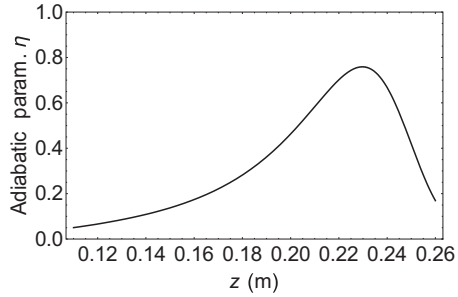

FIG. 3. The size of the adiabatic parameter, Eq. (9), along the electron flight path within the superconducting magnet, Fig. 4, for $E = 500$ keV.

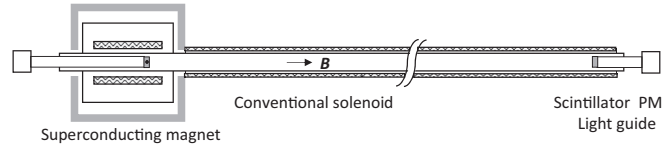

FIG. 4. Setup of the ToF apparatus. The ^{90}Sr-^{90}Y electron source is located inside the start detector on the left (small spot) at high field $B_1 = 2.5$ T. The stop detector is placed on the right at low field $B_2 = 0.022$ T. A light guide couples each detector to its photomultiplier (PM). In gray, the iron yoke of the magnet.

III. ToF INSTRUMENT

We first discuss the prototype ToF apparatus, shown in Fig. 4, built to test the feasibility of the proposed calibration method, and then present the results of some instrumental simulation studies.

A. ToF setup

The instrument consists of a superconducting high-field section and a conventional low-field section. For the high-field section with $B_0 = 3$ T, we use a 0.3 m long superconducting solenoid of 80 mm inner diameter, with a warm bore of 44 mm diameter, and an iron yoke of outer length 0.5 m and thickness 3 cm. In a similar setup, this solenoid had been used before to establish the electron point spread function after magnetic transport, see Ref. [24] and references therein. For the low-field section with $B_2 = 22$ mT, we prolonged the tube of the warm bore to a length of 5.0 m on one end of the magnet, and equipped it with a 4.42 m long water-cooled conventional solenoid of 65 mm inner diameter and 3000 turns.

The source and the start and stop detectors were located at $z_1 = 0.110$ m and $z_2 = 4.562$ m, respectively, the distance from the source to the center of the stop detector being $z_0 = z_2 - z_1 = (4.452 \pm 0.003)$ m. The 3 mm error of z_0 covers uncertainties both in thermal expansion of the long beam tube and in the position of electron emission and absorption.

Both detectors were flat plastic scintillators (Saint Gobain BC 440), 5 mm thick, with 40 mm diameter. Each scintillator was coupled to a photomultiplier (Hamamatsu R5504) of low magnetic-field sensitivity via an acrylic light guide of 40 mm diameter, of 0.5 m length for the start detector, and 0.2 m for the stop detector. To enhance light detection, the start scintillator was covered with a 10 μm thick reflecting foil of aluminized mylar.

As electron source we chose the pure β emitter ^{90}Sr, of half-life 29 years, with an activity of about 8 kBq. The ^{90}Sr β transition has an endpoint energy of 0.546 MeV, while the daughter β transition of ^{90}Y has its endpoint at 2.3 MeV, and an average energy of 927 keV. To obtain a start pulse for the ToF measurement, a drop of the source liquid was dried onto the bottom of a small, 2.5 mm deep hole of 5 mm diameter drilled into the center of the plastic scintillator, as shown in Fig. 5. In this way, to reach the surface of the start detector facing the stop detector, electrons had to penetrate at least 2.5 mm of scintillator, in which all βs of the low-energy ^{90}Sr transition were absorbed. Essentially all electrons leaving the scintillator produced a time signal in the start detector. Reference [10]

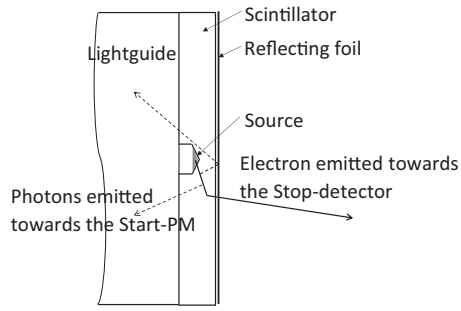

FIG. 5. Close-up of the start scintillator (shown on the left of Fig. 4).

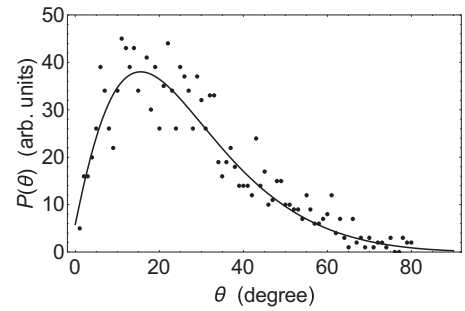

FIG. 6. Simulated initial angular distribution at the start detector, for electrons that reach the stop detector. The line is drawn to guide the eye.

discusses alternative methods to create a start pulse for ToF measurements.

For each detector, scintillation light is guided to a photomultiplier, where it is transformed into an analog signal. This signal then enters a linear fan-out, whose first output has to pass a constant fraction discriminator (CFD), while the second output is analyzed by a charge-to-digital converter (QDC). If the CFD signals of start and stop detectors are detected in coincidence, the data enter a so-called LogicBox, a home-developed data acquisition system [25]. The CFD output pulses are also used as input for a time-to-digital converter (TDC, Caen V775N), which provides the timing information. For energy analysis, the QDC provides a sample of an analog pulse every 10 ns, 64 samples altogether. An off-line fit to the samples of the integrated pulses finally yields the signal amplitudes. The fit is also used to crosscheck the measured ToF and to reject events, including multiple electron hits, by analyzing the goodness of fit. By this procedure, 7.8% of all events were rejected. We use a Landau distribution as a model for the time dependence of the photomultiplier pulses.

Exact timing is essential to the success of the ToF method. The clock of the TDC was calibrated by extending the signal paths of either one or the other channel by precisely known delays. Furthermore, the timing of both detectors is differing due to different photon yields, to different lengths of light guides and cables, and to the time walk of the discriminators. To measure this amplitude dependent timing offset δT and its width σ_T, we reduced the distance between both detectors from $z_0 = 4.45$ m to approximately 1 mm and repeated the measurement with an expected ToF of zero. After this procedure, the overall error of δT is estimated to 0.4 ns. We shall see, however, that this timing accuracy is not sufficient at the higher electron energies, and will present in Sec. IV A different method to determine δT precisely.

One shortcoming of our apparatus is the rather small inner diameter (44 mm) of its long electron flight tube. Let us make the (nonrealistic) assumption that the electrons leave the start detector at its center, that is, on the central field axis, to be transported adiabatically by the guide field to the stop detector. Then the electrons fit into the beam tube up to an energy of 420 keV. Beyond this energy, the maximum gyration diameter $2r_{20}$ at low field B_2 exceeds the tube radius $a = 22$ mm, and some electrons with large emission angle will hit the wall of the tube. If these electrons are backscattered from the wall, they inevitably hit the wall again, and in this way, are eliminated from the beam after a short distance along z. In this case, for $2r_{20} > a$, the solid angle of electron acceptance drops with increasing energy as

$$\Omega(E) = 1 - \sqrt{1 - [a/2r_{20}(E)]^2}. \tag{10}$$

In reality, the electrons' starting points have a radial distribution of finite diameter, and we must rely on numerical simulation.

B. Simulation studies

We did detailed numerical calculations and simulations on the properties of our apparatus. In principle, the ToF method requires no precise knowledge of the spectral and angular distributions of the electrons leaving the scintillator, because electron energy is measured separately by ToF, and the value of ToF is almost independent of the angle θ of emission. For the same reasons, the above-mentioned losses on the wall of the long flight tube are innocent. However, to be able to correct also for the small residual θ-dependent dispersion $\Delta\ell/\ell$ apparent in Fig. 2, and to investigate the effects of nonadiabaticity shown in Fig. 3, a simulation was performed with GEANT4, release 10.3.1 [26]. The required adaptions to the default settings [27] of GEANT were carefully taken into account. The simulation, based on 3×10^5 electron events, gives useful information on both spatial and angular distributions of electrons emitted from the start detector.

First, we simulated the spatial distribution of the electrons that leave the start detector through the surface facing the stop detector, in the geometry shown in Fig. 5. Due to electron straggling, it shows a mean radial spread about the field axis of 3.4 mm FWHM, and a spread of 10 mm at one-tenth-maximum. Remarkably, only those electrons starting with a radial distance below 2 mm reach the stop detector, the others are lost on the wall of the beam tube. Second, we simulated the initial angular distribution at the start detector of the electrons that do arrive at the stop detector. This distribution, after all wall losses and nonadiabatic changes of the electrons, is shown in Fig. 6. It is forward peaked, with a mean polar emission angle of $\langle\theta\rangle = 28^\circ$. Incidentally, the partial loss of events with high energies on the wall of the flight tube is also the reason why

a stop detector of thickness 5 mm was sufficient for electrons with energy below 1.1 MeV.

IV. ToF MEASUREMENTS AND RESULTS

In the following, we first list the existing methods of detector calibration. We then present our ToF data, obtained with the setup of Fig. 4, after various transformations. We indicate a method that permits to pin down the ToF offset to a few picoseconds. The energy response of our stop detector obtained from these data then is compared to theoretical expectations, and to a previous calibration based on conversion electron spectroscopy.

A. Methods of detector calibration

The calibration curve of an electron detector gives the relation between the electron kinetic energy E and the amplitude of the signal registered in the detection system. If the signals are stored in the channels numbered ch of a multichannel analyzer, then for the general case of a nonlinear response (with zero offset) we write this relation as

$$ch(E) = g(E)\,E, \tag{11}$$

with some gain or response function $g(E)$. For the ideal case of a linear detector response, the slope of the calibration curve is a constant g_0.

Various methods of energy calibration are in use for electrons in the energy range of neutron β decay, whose endpoint energy is 782 keV:

(i) The most popular method is the above-mentioned *in situ* calibration with monochromatic electrons of known energies, as obtained from a set of conversion electron emitters such as ^{109}Cd, ^{113}Sn, ^{139}Ce, ^{137}Cs, ^{207}Bi, and others, whose conversion lines cover the energy range up to 1 MeV. These sources are installed within the spectrometer, and are moved during data taking in regular time intervals into the line of sight of the detectors. However, this method is rather imprecise at low energies, because each such emitter has a multitude of conversion and Auger lines that introduce uncertainties into the calibration process. This was one of the reasons why the fit regions in previous neutron-decay experiments were chosen to start only at 300 keV, near the peak of the neutron β spectrum [7,19].

(ii) This *in situ* calibration method can be accompanied by more precise off-line calibration, using a magnetic momentum filter with a (uncalibrated) broadband electron source. Many different field configurations are possible for this purpose, see for instance Ref. [28].

(iii) A different off-line method measures angle and energy of Compton scattered γ rays, which create electrons of known energy within the bulk of the detector [29,30]. This method determines the bulk response of the detector material, but is insensitive to surface effects, such as dead layers in silicon detectors, or surface cracks in plastic scintillators, which may become important if the electron source lies outside the detector.

For PERC, electron energy calibration by ToF would combine several advantages of these methods:

(i) Like the conversion electron method (i), it can be done *in situ*, with the same apparatus as used in experiment.

(ii) Like the magnetic filter method (ii), it is sensitive to dead layers and imperfections of the detector surface.

(iii) Like the Compton method (iii), it is precise at low electron energies.

B. ToF data

To determine the gain function $g(E)$ of our scintillator, we recorded, for each event numbered $i = 1, \ldots, 73\,015$, a ToF value T_i from the start and stop signals, and a channel number ch_i of the coincident energy signal in the stop detector. The scatter plot "channel ch vs ToF T" in Fig. 7(a) shows the data points from our measurement at $B = 3$ T, for a ToF offset $\delta T = -92$ ps, as determined below, and with channel number zero set to signal height zero (no ch offset). To study systematic effects, similar measurements were also done at $B = 2$ T and 1 T. To guide the eye, the solid curve in the figure shows the relation between ch and T for a linear response $ch(T) = g_0 E(T)$, with $g_0 = 2.156$ ch/keV, and

$$E(T) = mc^2\Big[1 \Big/ \sqrt{1 - z_0^2/[c\,(T - T_0)]^2} - 1\Big], \tag{12}$$

as derived from Eqs. (4) and (5) under the assumption that path length $\ell = z_0$, or $\cos(\theta) = 1$, cf. Fig. 2. The thin vertical line in the figure gives the limiting value $T_0 = z_0/c = 14.85$ ns for direct flight at infinite energy, well separated from the minimum ToF at finite energies (15.1 ns at ^{90}Y end-point energy, 16.2 ns at neutron decay end point). The plot extends to $T = 45$ ns, which corresponds to $E = 30$ keV. One finds a certain number of data points with exceptionally low channel numbers, which make up about 3% of the total number of events. These points are due to electrons that backscatter from the stop detector and deposit only part of their energy in the scintillator.

The dashed curves in Fig. 7(a) are derived from the solid curve by adding and subtracting the expected one-σ standard deviations. The scatter of the data in the figure has two sources. The scatter in the horizontal along the T axis is due to the finite ToF resolution, which we assume to be Gaussian, determined below to $\sigma_T = (330 \pm 8)$ ps. The scatter in the vertical along the ch axis is due to the statistical Poissonian variation of the number N of photoelectrons (p.e.) registered in the photomultiplier of the stop detector, with standard deviation $\sigma_N = N^{1/2}$.

The sensitivity of our scintillation detector is measured to $\nu = (165 \pm 5)$ p.e./MeV, see below, with $N = \nu E$ for linear response (when we say linear response, we also mean zero offset). The statistical $\pm N^{1/2}$ scatter is significantly larger than the scatter due to electronic noise. The dashed line then is obtained by displacing each point on the solid curve by σ_T in the horizontal and by $\sigma_{ch} = (g_0/\nu)\sigma_N$ in the vertical, to reach a point at distance $(\sigma_T^2 + \sigma_{ch}^2)^{1/2}$. For the longer flight times T, the variance σ_T^2 from the ToF error can be neglected against the variance σ_{ch}^2 from photoelectron statistics, the crossover $\sigma_T^2 = \sigma_{ch}^2$ occurring at $T \approx T_0 + 3$ ns ≈ 18 ns where $E \approx 500$ keV.

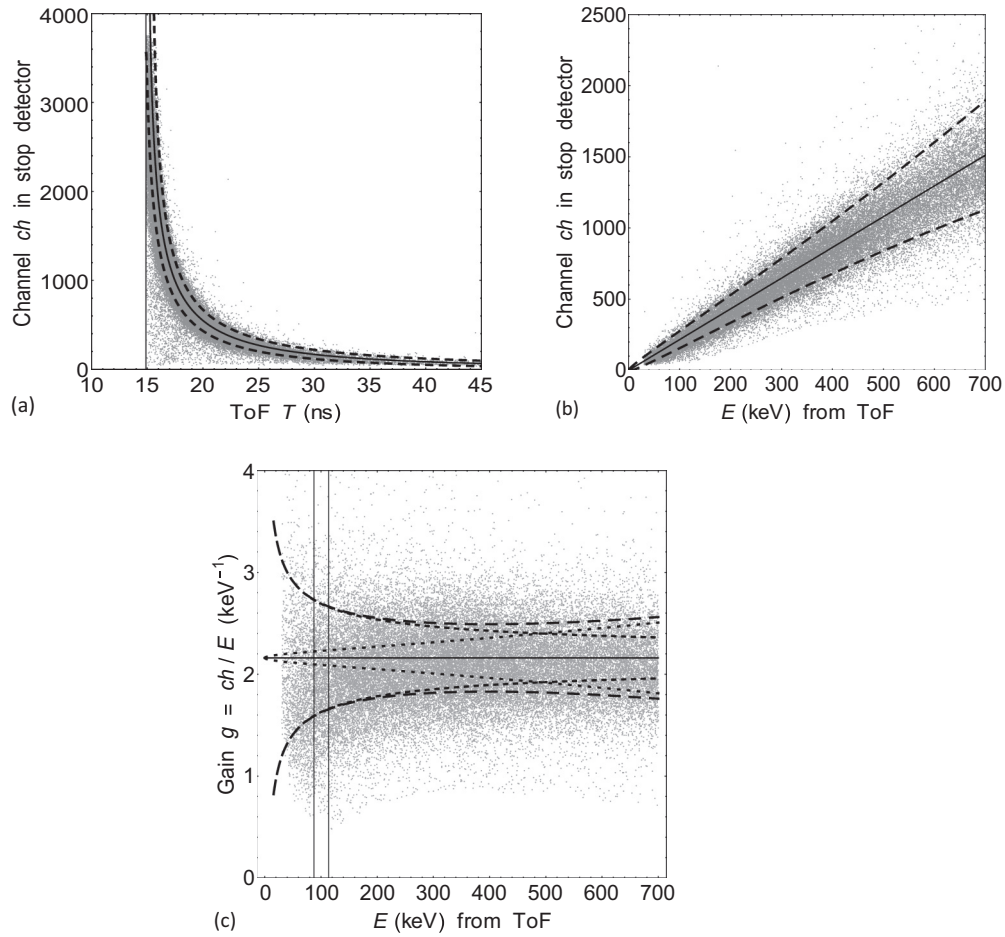

FIG. 7. (a) Scatter plot derived from the simultaneous measurement of electron ToF T and channel number ch in the energy sensitive stop detector. The thin vertical line indicates the lower time limit $T_0 = z_0/c$. (b) As (a), but with the abscissa changed to electron energy E, derived from T via Eq. (12). (c) As (b), but with the ordinate changed to gain $g = ch/E$. For details on the dashed one-sigma error contours, see text.

With the given errors, the reduced χ square of the data points in Fig. 7(a) is $\chi_o^2 = 0.91$. With the low-lying backscatter events removed, this reduces to $\chi_o^2 = 0.80$, which may indicate that error estimates are slightly conservative.

Next we transformed the coordinates of the figure into those of a conventional calibration curve, channel ch vs energy E, shown in Fig. 7(b), by using $E(T)$ from Eq. (12). The solid line is the linear calibration curve $ch = g_0 E$, with g_0 as in Fig. 7(a). The vertical scatter in ch is the same as before, while the previous ToF scatter leads to a horizontal energy scatter $\sigma_E = |dE/dT|\sigma_T$, where

$$\frac{dE}{dT} = -\frac{c}{z_0}\frac{[E(E+2mc^2)]^{3/2}}{m^2c^4}. \tag{13}$$

The dashed curves in Fig. 7(b) show again the one standard total deviations $\pm(\sigma_E^2 + \sigma_{ch}^2)^{1/2}$. Only energies up to 700 keV, with $\beta = 91\%$, are used in the plot, because beyond this energy the ToF method becomes imprecise.

To recognize nonlinearities in the calibration curve, we transformed the data points once more, changing the coordinates to "gain $g = ch/E$ vs E", see Fig. 7(c). In this case, for a linear detector response, the data points should scatter in the vertical about a constant value g_0. To guide the eye, the horizontal line in the figure shows the same constant gain $g_0 = 2.156\,\mathrm{ch/keV}$ as before.

In Fig. 7(c), the widely dashed curves show again the one standard deviation from the horizontal line $g = g_0$. Under linear response, the scatter in the horizontal with standard deviation $\sigma_E = |dE/dT|\,\sigma_T$ has no effect on g_0. Instead, σ_E enters the vertical gain error $\sigma_g = g_0[(\sigma_E/E)^2 + (\sigma_{ch}/ch)^2]^{1/2}$. The dotted and the narrowly dashed curves show separately the individual contributions of σ_E and σ_{ch}, respectively. Points with a gain that is more than about three standard deviations below g_0, mostly due to backscattering, are discarded in Figs. 7(b) and 7(c).

In our data treatment, as a further refinement we included the effect of the small residual dispersion of path lengths $\Delta\ell/\ell$, which vary with initial emission angle θ as was shown by the solid line in Fig. 2. To this end, we corrected the flight times T of the individual data points to

$$T'(\theta) = [1 - \Delta\ell(\theta)/z_0]\,T + \delta T \tag{14}$$

and averaged our calculations over θ, using the angular distribution of Fig. 6. In Eq. (14), we also foresee a constant residual ToF offset δT.

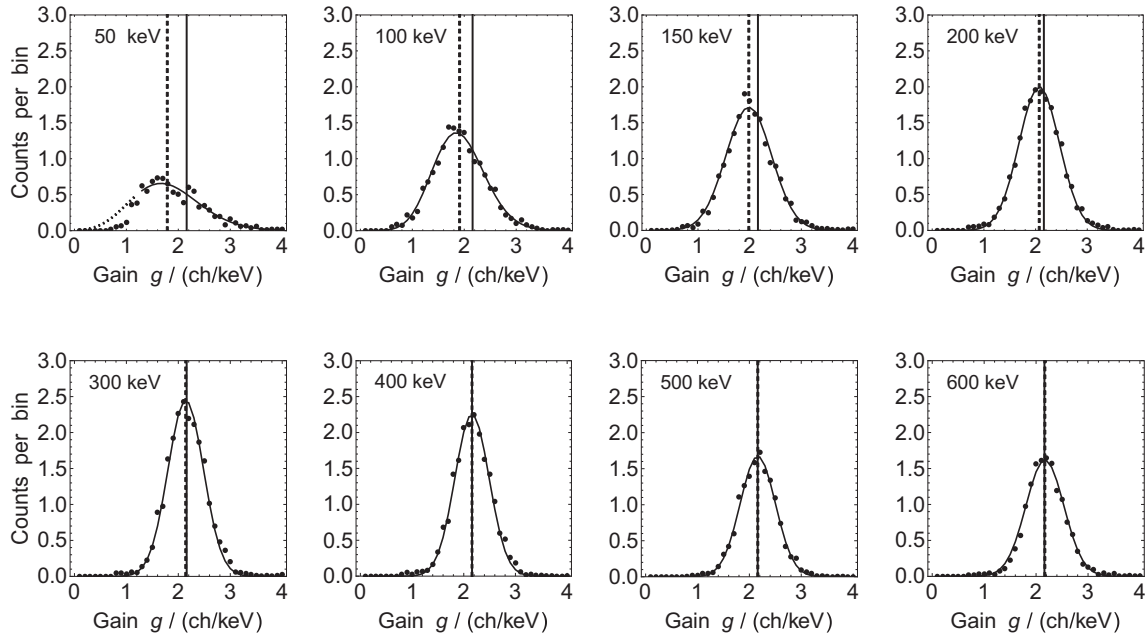

FIG. 8. Counts per bin as a function of gain g, obtained from vertical cuts in Fig. 7(c), for selected electron energies E. Solid curves: fits to the data. Dashed vertical lines: mean values of the distribution. Solid vertical lines: saturation gain $g_0 = 2.156\,\mathrm{ch/MeV}$. At low energies, shown in the panels of the top row, the mean values steadily move into the direction of g_0. At high energies, shown in the panels of the bottom row, the distributions remain centered at g_0. Bin widths are $\Delta E = 25\,\mathrm{keV}$ and $\Delta g = 0.1\,\mathrm{ch/keV}$.

C. Signature of nonlinearity

When looked upon from a certain distance, the horizontal stripe of data points in Fig. 7(c) seems to bend down for the lower energies, which hints at a nonlinearity of the gain function $g(E)$. To investigate this more closely, we look at the distribution of data points along vertical bands of constant energy, parallel to the g axis. The two vertical lines in Fig. 7(c) indicate one such band. In more detail: for an energy band of width ΔE, centered at energy E_i, we determine the contents of the successive gain bins of constant width Δg and of size $\Delta E \times \Delta g$. We then plot the number of events in these bins, and determine the mean gain of this distribution. This gives us the gain function $g(E_i)$ of the plastic scintillation detector at energy E_i. The bin widths are chosen to $\Delta E = 25\,\mathrm{keV}$ along the horizontal and $\Delta g = 0.1\,\mathrm{ch/keV}$ along the vertical axis. These bins then cover the plane of Fig. 7(c) without overlap.

Figure 8 shows the resulting distributions of event numbers within these bands, for a subset of eight different energies E_i, which are indicated in the top left of each panel. The dots in the figure give the bin contents, while the curves are fits to Gaussians (Poissonians for energies below 200 keV where timing errors are negligible), with predetermined total widths $\sigma_g(E_i)$. The only fit parameters are position (= mean) and amplitude of the distribution. The mean values of the curves give the gains $g(E_i)$ at energies E_i, indicated by the dashed vertical lines. The solid vertical lines indicate the fixed saturation gain g_0. In the first panel with $E = 50\,\mathrm{keV}$, the low-energy cutoff of the trigger function of the stop detector becomes visible. Therefore, in this first panel, the fit to the data begins not at zero, but at $g = 1.2\,\mathrm{ch/keV}$.

In the top panels of the figure, energies increase from 50–200 keV in steps of 50 keV, with E in the center of the band. In the bottom panels, energies increase from 300–600 keV in steps of 100 keV. We see that, with increasing energy, the positions $g(E_i)$ (dashed vertical line) move asymptotically towards a constant gain g_0 (solid vertical line). The typical reduced χ squares of the fits in Fig. 8 vary between 0.7 and 1.7, with 38 degrees of freedom (dof).

We can do the same fits with the two width parameters, number of photoelectrons, and ToF resolution as additional free parameters. The results are $\nu = (165 \pm 5)\,\mathrm{p.e./MeV}$, and $\sigma_T = (330 \pm 8)\,\mathrm{ps}$. These additional parameters do not deteriorate the fit results for the position parameters $g(E_i)$ in Fig. 8, because they are uncorrelated to g to better than 10^{-6} at 100 keV and beyond (the same is true for the amplitudes of the curves). The result for ν is consistent with results from ^{207}Bi calibration measurements, and the value for σ_T is somewhat better than the $\sigma_T = 400\,\mathrm{ps}$ conservatively estimated from the spread of ToF signals, as was described in Sec. III. Within error, the $g(E_i)$ remain the same when detector sensitivity ν is varied between 120 and 220 p.e./MeV, and when instrumental ToF error σ_T is varied between 0.2 and 0.5 ns.

However, we have to add another important step, because the time calibration procedure described in Sec. III turned out to be insufficient for our purposes. Certainly, the strong nonlinearity seen at low energies (long flight times) is rather stable against variations of the offset δT. On the other hand, for the larger energies, beyond about 400 keV where $T - T_0$ falls below 3 ns, the gain function $g(E)$ becomes rather unstable under variation of δT. Even worse, in spite of our efforts to balance the timing in both detector channels (described in Sec. III A), there remained an overall timing offset of 1.115 ns, probably due to some bookkeeping error. This offset was easily visible in the high-energy ToF data [near the vertical line in

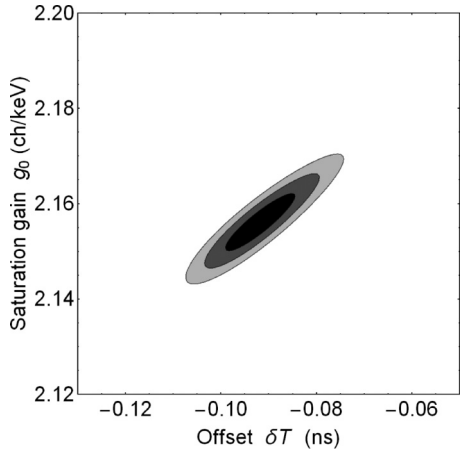

FIG. 9. The timing offset δT and the saturation gain g_0 are fixed by the requirement that the normalized gain saturates to $g(E) = g_0$ for the higher electron energies E. Shown are the 1, 2, and 3 σ χ-square contours for deviations of the gain function $g(E)$ from a constant g_0 for the higher electron energies. The χ-square minimum, $\chi^2 = 15.2$ with 9 dof, lies at $\delta T = -92$ ps and $g_0 = 2.156$ ch/keV.

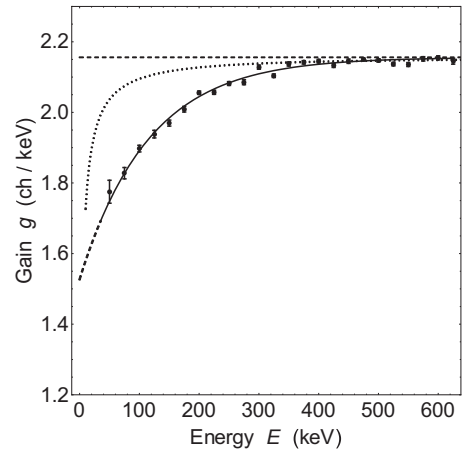

FIG. 10. The gain function $g(E)$ of the plastic scintillator, as derived from Fig. 8. Below 350 keV, a strong nonlinearity appears, with g significantly deviating from its saturation value g_0. The solid curve is an empirical fit to Eq. (15). The dotted curve shows the expectation from theory, Eq. (16).

Fig. 7(a)], and we removed it beforehand from the data, though still keeping an eye on a possible residual δT in Eq. (14).

There is a simple way out of these timing problems: We postulate that detector nonlinearities occur only at the lower energies, that is, we require that the gain $g(E)$ saturates at higher energies and reaches a constant value g_0. This postulate seems to hold for the scintillation process [31], and has, to our knowledge, never been called into question. There still might be nonlinearities in the subsequent signal processing modules, due to bandwidth limitations. However, such electronics induced nonlinearities were tested separately and were found to be small in the energy interval tested for saturation. As we shall see, this postulate of saturation, when applied to our data, fixes δT and g_0 and drastically reduces their errors.

To assure that detector response saturates at high energies, we varied the timing offset δT and the saturation gain g_0 and calculated, for energies from 350–625 keV, the χ square for the deviation of the gain function $g(E)$ from a constant g_0. Figure 9 shows the 1, 2, and 3-σ contours of χ^2 as a function of δT and g_0. By this procedure, the time offset is fixed to $\delta T = (-92 \pm 7)$ ps, and the saturation gain to $g_0 = (2.156 \pm 0.006)$ ch/keV, with a reduced χ square of $\chi^2_{0\,\mathrm{sat}} = 3.0$ with 9 dof, where the subscript "sat" stands for saturation test. Between 0.3 and 1.0 MeV, this result is, within errors, stable agains variations of the fit interval. The curves in Fig. 8 had been derived with these optimum values of δT and g_0.

D. Gain function of the scintillator

Figure 10 shows the detector response or gain function obtained in the described manner. The errors shown are the fit errors for the positions of the distributions in Fig. 8. To guide the eye and to quantify our result, an exponential approach to saturation at high energies is fitted to the data points,

$$g = g_0(1 - q\ \mathrm{e}^{-E/E_c}), \tag{15}$$

with two free parameters, the deviation q from linearity at $E = 0$, and a characteristic energy E_c, with the result $q = 0.29 \pm 0.03$ and $E_c = (115 \pm 8)$ keV, with a reduced χ square of 3.0 with 22 dof. (In fact, shown is not g, but $0.995g$, to better approach the dotted asymptotic Birks curve.)

A known source of nonlinearities at low energy is the light yield L of the scintillation process, described by Birks' law [32]

$$\frac{dL}{dE} = \frac{1}{1 + kB\ dE/dx}. \tag{16}$$

A value of the Birks constant kB was measured independently for a similar scintillator (Saint Gobain BC 404) with the Compton apparatus of Ref. [30], and was found to be of the order of 120 nm/keV. The dotted curve in Fig. 10 shows the gain function expected from Eq. (16) with this value of kB, and with dE/dx for plastic scintillators (vinyltoluene based) from [33]. Its nonlinearity is much smaller than that seen in our measurement.

As Birks' formula accounts for the bulk properties of a scintillator, it is likely that this deviation is due to effects specific to our setup. One might suspect that this deviation is due to a dead layer, caused, for instance, by microcracks in the surface of the plastic scintillator. However, this seems unlikely, because a dead layer of several μm thickness would produce an additional cutoff at low energy not visible in the data. Possibly, the deviation is due to additional electronic effects at low energies, but for an *in situ* correction one does not really have to know the origin of the deviation as long as it is the same as in the data under correction, and not linked to the ToF method itself.

On the other hand, for energies beyond 650 keV, not shown in Fig. 10, the gain decreases almost linearly by 2% per additional 100 keV. This loss is due to a partial saturation of the QDC. At energies beyond 1.1 MeV, also the finite thickness of the stop detector starts playing a role. More generally, when electron velocities approach the speed of light, the sensitivity

TABLE I. The shape of the detector response in Fig. 10 is, within errors, insensitive to the shape of the underlying angular distribution of the electrons (first two columns), and to nonadiabatic effects (last line). The quantity $\langle \Delta\ell/\ell \rangle$ (third column) gives the path length changes (Fig. 2), averaged over these angular distributions. The nonlinearity q of the gain function $g(E)$ at $E = 0$ and the characteristic energy E_c (last two columns) are from fits to Eq. (15). "Simulated" refers to the angular distribution of Fig. 6, as does "Extreme", but with a 30 times enlarged $\langle \Delta\ell/\ell \rangle$.

Angular distribution	Mean emission angle $\langle\theta\rangle$	$\langle \Delta\ell/\ell \rangle$ for path lengths ℓ	Nonlinearity q	Characteristic energy E_c (keV)
Cigar	0°	0	0.30(3)	112(8)
Simulated	28°	0.3%	0.29(3)	115(8)
Isotropic	57°	1.1%	0.29(3)	112(8)
Pancake	90°	3.4%	0.30(3)	116(8)
Extreme	28°	10%	0.26(3)	111(12)

of the ToF method is getting lost. For ToF applications in neutron decay, however, with its 782 keV endpoint energy, these deviations at high energy are not relevant.

To find out whether the gain function in Fig. 10 is sensitive to deviations from the initial angular distribution of Fig. 6, we repeated the evaluation for several other emission patterns, with different flight path corrections $\Delta\ell(\theta)$ in Eq. (14). Besides the distribution given in Fig. 6 (depicted as "Simulated"), we used a strongly prolate distribution ($\theta \approx 0°$) where $\ell \approx z_0$ ("cigar"), a strongly oblate distribution ($\theta \approx 90°$) where ℓ deviates most strongly from z_0 ("pancake"), as well as an isotropic distribution, see Table I. For all these angular patterns, listed in the first column of Table I, the values for q and E_c come out practically the same, and therefore the shape of the respective gain functions looks practically the same as that shown in Fig. 10, with about the same χ square. Furthermore, nonadiabatic effects, Fig. 3, may induce an additional broadening of the path length distribution. To check this, we increased the path length dispersion to an extreme value $\Delta\ell/\ell = 10\%$, 30 times stronger than expected for the simulated distribution, Fig. 6, under adiabatic transport. Again, the changes of the gain function remain within error, see the last line in Table I. Evidently, our saturation requirement forces detector response always into the same appearance.

To give an indication of the status of the conventional *in situ* calibration method, Fig. 11 shows the typical result of a calibration with a set of conversion electron emitters and their Auger electrons. The figure is based on the data given in Ref. [34] for a plastic scintillator of a similar type (Bicron BC-400) used in an earlier experiment. Application of the same exponential fit, Eq. (15), to these data gives $q = 0.23 \pm 0.04$ and $E_c = (134 \pm 17)$ keV. Note that more recent calibration runs somewhat improved on this by simultaneous fits to all conversion and Auger lines, sometimes together with fits to the β spectrum of neutron decay.

E. Outlook

One drawback of our ToF calibration method certainly is that we must assume gain saturation in order to pin down the timing offset δT. To avoid this, one must either do a better direct measurement of δT, or try to obtain δT by extensive modeling of the apparatus, or choose a hybrid procedure and complement ToF calibration at low energies (where the δT uncertainty is negligible) by conventional calibration with conversion electrons at the higher energies.

How well must δT be known in order to recognize a deviation from saturation? To find out, we imposed additional linear slopes onto the experimental gain curve $g(E)$, as derived from Fig. 8. Our data evaluation program does not recognize such a slope, because it readjusts δT and g_0 until saturation is reestablished. However, from the shift in δT that is required to iron out such slopes we can deduce how well the time offset δT must independently be known in order to recognize such a loss of saturation. For relative slopes of size $\pm 0.5\%$ per 100 keV, the required shifts of δT and g_0 are given in Table II.

Also shown in Table II are the nonlinearities q and characteristic energies E_c resulting from this operation. Within error, they come out the same as in Table I. These shifts in δT tell us that a time resolution of about 20 ps is desirable to pin down a loss of saturation with reasonable precision. This time resolution is difficult to achieve by direct measurement, therefore we next discuss the present status of modeling for our prototype apparatus.

We did a calculation of the gain function, based on a full simulation of the apparatus. To find $g(E)$, we actually remained in the ToF domain and applied the following

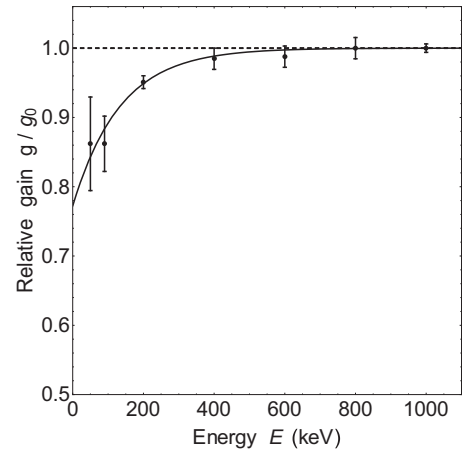

FIG. 11. Result of a conventional energy calibration of a plastic scintillator with a set of conversion electron sources. The two entries at the lowest energies are from the Auger electrons accompanying the electron conversion process. Adapted from Ref. [34].

TABLE II. Effect of additional slopes in the gain curve $g(E)$ on the time offset δT. For details see text.

Angular distribution	Slope of gain $g(E)$	Shift of δT(ps)	Shift of g_0(ch/keV)	Nonlinearity q	Characteristic energy E_c(keV)
Simulated	+0.5%/100 keV	−92(9)	−0.015(8)	0.29(3)	115(8)
	−0.5%/100 keV	+107(9)	+0.024(8)	0.30(3)	114(8)

correction functions in the model calculation. First, the theoretical energy spectrum within one ToF slice was calculated, using Eq. (12). In the next step, the scintillator nonlinearity expected from Birks' theory was applied, with $kB = 120\,\text{nm/keV}$. The resulting spectrum then was convoluted with a Poisson broadening function and with the photomultiplier response function, which is a chain of Poissonian responses of the successive stages of the photomultiplier. Finally, the measured timing offset δT was applied to the theoretical spectrum, and the likelihood was used to obtain a fitted model. To determine the nonlinearity, we also performed systematic studies on the influence of the magnetic fields, using measurements at $B_0 = 1$, 2, and 3 T.

In these calculations, the ToF offset δT was obtained with a precision of roughly 50 ps. This is not yet sufficient for our results, and should be about three times more precise. We expect that, with PERC, this result for δT can be considerably improved, for several reasons. First, PERC has both peak field B_0 and flight length z_0 doubled, which reduces path length dispersion $\Delta\ell$ and doubles the measured ToF T. Second, there will be no wall losses, which will improve statistics at similar dead time. Finally, there will be no iron yoke near the electron flight path, and no large nonadiabatic effects.

Our finding underlines the necessity to accompany neutron decay studies with PERC by precise in situ calibration measurements with the ToF method. The same ToF method can also be applied to other types of electron detectors, like SiLi detectors, though, with a time resolution lower than that of a plastic scintillator.

V. CONCLUSIONS

In the past, electron time-of-flight (ToF) played almost no role in β-decay studies. We showed that electron ToF can be a useful tool, in particular for the characterization of electron detectors. It permits detector calibration with high precision in the whole energy range relevant for neutron decay, including electron energies well below 100 keV, where conventional calibration methods fail.

ACKNOWLEDGMENTS

This work was supported by the Deutsche Forschungsgemeinschaft, DFG, Priority Programme 1491. We thank O. Hornberger for the diligent winding of the long solenoid.

[1] B. R. Holstein, Precision frontier in semileptonic weak interactions: Theory, J. Phys. G **41**, 110301 (2014).
[2] V. Cirigliano, M. Gonzáles-Alonso, and M. L. Graesser, Non-standard charged current interactions: beta decays versus the LHC, J. High Energy Phys. 02 (2013) 046.
[3] V. Cirigliano, S. Gardner, and B. R. Holstein, Beta decays and non-standard interactions in the LHC era, Prog. Part. Nucl. Phys. **71**, 93 (2013).
[4] T. Bhattacharya, V.Cirigliano, S. D. Cohen, A. Filipuzzi, M. González-Alonso, M. L. Graesser, R. Gupta, and Huey-Wen Lin, Probing novel scalar and tensor interactions from (ultra)cold neutrons to the LHC, Phys. Rev. D **85**, 054512 (2012).
[5] K. K. Vos, H. W. Wilschut, and R. G. E. Timmermans, Symmetry violations in nuclear and neutron β; decay, Rev. Mod. Phys. **87**, 1483 (2015).
[6] D. Dubbers and M. G. Schmidt, The neutron and its role in cosmology and particle physics, Rev. Mod. Phys. **83**, 1111 (2011).
[7] D. Mund, B. Märkisch, M. Deissenroth, J. Krempel, M. Schumann, and H. Abele, Determination of the Weak Axial Vector Coupling $\lambda = g_A/g_V$ from a Measurement of the β-Asymmetry Parameter A in Neutron Beta Decay, Phys. Rev. Lett. **110**, 172502 (2013).
[8] M. P. Mendenhall *et al.*, Precision measurement of the neutron β-decay asymmetry, Phys. Rev. C **87**, 032501 (2013).
[9] T. E. Chupp, R. L. Cooper, K. P. Coulter, S. J. Freedman, B. K. Fujikawa, A. García, G. L. Jones, H. P. Mumm, J. S. Nico, A. K. Thompson, C. A. Trull, F. E. Wietfeldt, and J. F. Wilkerson, Search for a T-odd, P-even triple correlation in neutron decay, Phys. Rev. C **86**, 035505 (2012).
[10] D. Dubbers, Characterization of electron detectors by time-of-flight in neutron β decay experiments, arXiv:1611.00192.
[11] G. Beamson, H. Q. Porter, and D. W. Turner, The collimating and magnifying properties of a superconducting field photoelectron spectrometer, J. Phys. E **13**, 64 (1980).
[12] P. Kruit and F. H. Read, Magnetic field paralleliser for 2π electron-spectrometer and electron-image magnifier, J. Phys. E **16**, 313 (1983).
[13] A. M. Rijs, E. H. G. Backus, C. A. de Lange, N. P. C. Westwood, and M. H. M. Janssen, 'Magnetic bottle' spectrometer as a versatile tool for laser photoelectron spectroscopy, J. Electron. Spectroscopy Related Phenomena **112**, 151 (2000).
[14] S. Baeßler, F. AyalaGuardia, M. Borg, F. Glück, W. Heil, G. Konrad, I. Konorov, R. Munoz Horta, G. Petzoldt, D. Rich, M. Simson, Yu. Sobolev, H.-F. Wirth, and O. Zimmer, First measurements with the neutron decay spectrometer aSPECT, Eur. Phys. J. A **38**, 17 (2008)
[15] E. W. Otten and C. Weinheimer, Neutrino mass limit from tritium β decay, Rep. Prog. Phys. **71**, 086201 (2008).
[16] J. Bonn, L. Bornschein, B. Degen, E. W. Otten, and Ch. Weinheimer, A high resolution electrostatic time-of-flight

spectrometer with adiabatic magnetic collimation, Nucl. Instrum. Methods Phys. Res., Sect. A **421**, 256 (1999).
[17] J. F. Amsbaugh *et al.*, Focal-plane detector system for the KATRIN experiment, Nucl. Instrum. Methods A **778**, 40 (2015).
[18] K. E. Norell, P. Baltzer, B. Wannberg, and K. Siegbahn, A new magnetic time-of-flight spectrometer for electron spectroscopy, Nucl. Instrum. Methods **227**, 499 (1984).
[19] B. Plaster *et al.*, Measurement of the neutron β-asymmetry parameter A_0 with ultracold neutrons, Phys. Rev. C **86**, 055501 (2012).
[20] M. Schumann, M. Kreuz, M. Deissenroth, F. Glück, J. Krempel, B. Märkisch, D. Mund, A. Petoukhov, T. Soldner, and H. Abele, Measurement of the Proton Asymmetry Parameter in Neutron Beta Decay, Phys. Rev. Lett. **100**, 151801 (2008).
[21] M. Schumann, T. Soldner, M. Deissenroth, F. Glück, J. Krempel, M. Kreuz, B. Märkisch, D. Mund, A. Petoukhov, and H. Abele, Measurement of the Neutrino Asymmetry Parameter B in Neutron Decay, Phys. Rev. Lett. **99**, 191803 (2007).
[22] G. Konrad *et al.* (The PERC Collaboration), Neutron decay with PERC: A progress report, J. Phys. Conf. Ser. **340**, 012048 (2012).
[23] D. Dubbers, H. Abele, S. Baeßler, B. Märkisch, M. Schumann, T. Soldner, and O. Zimmer, A clean, bright, and versatile source of neutron decay products, Nucl. Instrum. Methods A **596**, 238 (2008).
[24] D. Dubbers and U. Schmidt, Generation of narrow peaks in spectroscopy of charged particles, Nucl. Instrum. Methods A **837**, 50 (2016).
[25] E. Rubio, http://ew-dev.physi.uni-heidelberg.de/~rubio/LogicBox.
[26] J. Allison *et al.*, Recent developments in GEANT4, Nucl. Instrum. Methods A **835**, 186 (2016).
[27] S. H. Kim, M. G. Pia, T. Basaglia, M. C. Han, G. Hoff, C. H. Kim, and P. Saracco, Validation Test of Geant4 Simulation of Electron Backscattering, IEEE T. Nucl. Sci. **62**, 451 (2015).
[28] K. Siegbahn, *Alpha. Beta and Gamma Spectroscopy* (North Holland, Amsterdam, 1968), Vol. I, Chap. III.
[29] M. N. Péron and P. Cassette, COCO, a Compton coincidence experiment to study liquid scintillator response in the 1–20 keV energy range, Nucl. Instrum. Methods A **353**, 41 (1994).
[30] C. Aberle, C. Buck, F. X. Hartmann, S. Schönert, and S. Wagner, Light output of Double Chooz scintillators for low energy electrons, JINST **6**, P11006 (2011).
[31] J. B. Birks, *The Theory and Practice of Scintillation Counting* (Pergamon, Oxford, 1964).
[32] J. B. Birks, The specific fluorescence of anthrazene and other organic materials, Phys. Rev. **84**, 364 (1951).
[33] http://physics.nist.gov/Star.
[34] H. Mest, Measurement of the β-asymmetry in the decay of free polarized neutrons with spectrometer PERKEOIII, Ph.D. thesis, Heidelberg, 2011.